Mon. Not. R. Astron. Soc. **000**, 1–14 () Printed 18 June 2010 (MN LATEX style file v2.2)

# Multi-dimensional modelling of X-ray spectra for AGN accretion-disk outflows III: application to a hydrodynamical simulation

S. A. Sim[1], D. Proga[2] L. Miller[3], K. S. Long[4], T. J. Turner[5]
[1]*Max-Planck-Institut für Astrophysik, Karl-Schwarzschildstr. 1, 85748 Garching, Germany*
[2]*Department of Physics, University of Nevada, Las Vegas, NV 89154*
[3]*Dept. of Physics, University of Oxford, Denys Wilkinson Buiding, Keble Road, Oxford OX1 3RH, U.K.*
[4]*Space Telescope Science Institute, 3700 San Martin Drive, Baltimore, MD 21218, U.S.A*
[5]*Dept. of Physics, University of Maryland Baltimore County, 1000 Hilltop Circle, Baltimore, MD 21250, U.S.A*



18 June 2010

**ABSTRACT**
We perform multi-dimensional radiative transfer simulations to compute spectra for a hydrodynamical simulation of a line-driven accretion disk wind from an active galactic nucleus. The synthetic spectra confirm expectations from parameterized models that a disk wind can imprint a wide variety of spectroscopic signatures including narrow absorption lines, broad emission lines and a Compton hump. The formation of these features is complex with contributions originating from many of the different structures present in the hydrodynamical simulation. In particular, spectral features are shaped both by gas in a successfully launched outflow and in complex flows where material is lifted out of the disk plane but ultimately falls back. We also confirm that the strong Fe K$\alpha$ line can develop a weak, red-skewed line wing as a result of Compton scattering in the outflow. In addition, we demonstrate that X-ray radiation scattered and reprocessed in the flow has a pivotal part in both the spectrum formation and determining the ionization conditions in the wind. We find that scattered radiation is rather effective in ionizing gas which is shielded from direct irradiation from the central source. This effect likely makes the successful launching of a massive disk wind somewhat more challenging and should be considered in future wind simulations.

**Key words:** radiative transfer – methods: numerical – galaxies: active – X-rays: galaxies

## 1 INTRODUCTION

Estimates for the black hole mass ($M_{\rm bh}$) and bolometric luminosity ($L_{\rm bol}$) of the most luminous active galactic nuclei (AGN) suggest that they are accreting close to the Eddington rate, $\dot{M}_{\rm Edd}$. Under such conditions, radiation forces should play a role in determining the properties of the accretion disk atmosphere. In particular, since much of the luminosity of the inner regions of the disk is radiated in the ultraviolet (uv) part of the spectrum, a significant radiative force should arise owing to the large number of line transitions which occur in this spectral region. By analogy to hot star atmospheres, it is to be expected that radiation pressure due to ultraviolet line driving can exceed that due to electron scattering by factors up to $M_{\rm max} \sim 10^3$ (Castor et al. 1975; Stevens & Kallman 1990; Proga et al. 2000) under optimal conditions. Thus the radiation force due to spectral lines might be expected to affect the structure of a uv-bright accretion disk for luminosities as small as $\sim M_{\rm max}^{-1}\, L_{\rm Edd}$.

In luminous hot stars line-driving by the uv radiation field is able to launch fast winds with terminal velocities comparable to the escape speed from the stellar photosphere (e.g. Castor et al. 1975; Friend & Abbott 1986; Pauldrach et al. 1986). For AGN accretion disks, launching of a wind is hindered by the large luminosity of ionizing X-ray radiation produced in the vicinity of the central black hole. Line-driving becomes rapidly less efficient as the ionization state of the gas is raised (see e.g. Stevens & Kallman 1990; Arav et al. 1994). As a consequence, for luminosities around $0.001 \lesssim L/L_{\rm Edd} \lesssim 0.1$, line-driving is unable to launch a successful wind but should give rise to a topologically complex "failed wind" in which material is lifted out of the disk plane but, due to over-ionization by the X-ray radiation, does not reach escape speed (Proga & Kallman 2004; hereafter PK04, see also Proga et al. 2000; Proga 2005). Above $L \sim 0.1\ L_{\rm Edd}$, however, numerical simulations suggest that even the ionizing X-ray flux may be unable to fully suppress the launching of a line-driven disk wind. In particular, PK04 performed radiation-hydrodynamical simulations for an accretion disk around a supermassive black hole ($M_{\rm bh} = 10^8$ M$_\odot$). They investigated the case of $L \sim 0.5 L_{\rm Edd}$ assuming that 10 per cent of the luminosity was radiated as X-rays from a centrally concentrated source. This central source could ionize the gas but was

not included as a source of radiation pressure – the line driving force was supplied by the uv radiation of the accretion disk. Their simulations predicted that, despite the ionizing effects of the X-ray radiation, a significant mass flux was successfully accelerated that formed an outflow with terminal velocity comparable to the escape speed from the inner accretion disk.

The flow structure found by PK04 is complex and significantly time-variable but it is persistent and characterized by three regimes: a cold dense equatorial outflow, a hot diffuse polar flow and a thin layer of moderate density rapidly outflowing warm material at intermediate inclination. The typical mass-loss rate of the flow was $\sim 0.1-0.2$ M$_\odot$ yr$^{-1}$, this being dominated by the warm, rapid outflow component. In addition, the simulation predicts a dense "failed wind" region above the inner disk which plays a pivotal part in determining the wind structure owing to both the ram pressure it exerts and its potential role in shielding the gas in the outer regions of the flow from the ionizing X-ray radiation. We note, however, that PK04 assumed that all the X-ray radiation is emitted by a point source and they neglected scattering or reprocessing of X-rays in the flow. As will be discussed later, this likely overestimates the ease with which the "failed wind" can shield the outer parts of the flow.

Given the geometrical and kinematic complexity of the PK04 wind structure, predicting its spectroscopic signatures is challenging. But given the large mass-loss rate of the warm stream and the significant covering fraction of the "failed wind", it is certainly expected that observational signatures will arise. Since a large fraction of the material around the inner parts of the flow should be strongly ionized, the clearest signatures of the absorption and emission from the wind structure may be expected to manifest in the X-ray band. Schurch et al. (2009) performed radiation transfer calculations for snapshots of the wind structure obtained by PK04, again assuming that all X-rays are emitted by a single point source. They confirmed that, depending on the observer's orientation, the wind structures could strongly absorb X-ray radiation and therefore imprint observable signatures. Although an important step, the Schurch et al. (2009) study suffers from the shortcoming that the radiative transfer code used (XSCORT; Schurch & Done 2007) is only one-dimensional. Thus, although they could study the absorption properties of the disk wind, they did not realistically address the role of the wind in producing/shaping emission features.

We have developed a multi-dimensional Monte Carlo radiative transfer code which is able to compute orientation-dependent spectra for wind models taking proper account of scattering and reprocessing of radiation in the outflow (Sim 2005, Sim et al. 2008; hereafter Paper I, Sim et al. 2010; hereafter Paper II). Applying this code to simply-parametrized disk wind geometries has shown that scattered/reprocessed radiation has a very important role in the formation of the X-ray spectrum and that outflow models may have the capacity to explain a wide variety of X-ray spectroscopic features (see Papers I and II). In particular, highly blue-shifted absorption features, as have been reported in a number of luminous AGN (see section 6.1 of Turner & Miller 2009 for a recent review), appear for a subset of inclination angles while Fe K$\alpha$ emission is predicted for all observer orientations. The line emission is typically broad and can develop somewhat red-skewed line wings (Papers I and II) owing to the effects of Compton scattering in the flow (see e.g. Laming & Titarchuk 2004; Laurent & Titarchuk 2007; Titarchuk et al. 2009).

To date, however, we have only applied our Monte Carlo code to parametrized outflow models with imposed mass-loss rates and flow geometries. Although such simple models provide a convenient means to investigate the formation of the X-ray spectrum in an outflow, they do not adequately represent the full complexity of the wind structures found in the radiation-hydrodynamical simulations mentioned above. In particular, they adopt a very simple velocity law (which is not dynamically consistent with any particular launching/acceleration mechanism) and assume that all the material that is lifted out of the disk plane is part of a flow that successfully escapes from the system. Thus, at best, the parametrized wind models might represent components similar to the warm outflow in the PK04 simulation but they neglect any other structures which accompany it (e.g. the "failed wind"). It is therefore important to investigate whether there are characteristic differences between the X-ray spectra obtained from simplified wind models and dynamically self-consistent flow models since these are relevant to the quantitative interpretation of observations.

Here we take the step of connecting our studies of the formation of X-ray spectra in multi-dimensional flows (Papers I and II) to a physically motivated disk wind model (PK04). The objectives of this study are two fold. First, by computing synthetic X-ray spectra for a hydrodynamical simulation we can more reliably investigate which spectral features can plausibly form in disk winds and assess how well synthetic spectra from parametrized models (such as those used in Paper II) correspond to what might be expected from more realistic flow structures. Second, by using a radiative transfer scheme that readily incorporated true absorption, scattering and reprocessing of radiation in the wind, we can begin to assess the importance of scattered radiation for the physical processes at work in a line-driven wind. We begin, in Section 2 with a description of the setup of our simulations. The results are presented in Section 3 and their implications discussed in Section 4.

## 2 MODEL SETUP

### 2.1 Radiation-hydrodynamical wind simulation

To provide a set of self-consistent gas properties for our Monte Carlo radiative transfer simulations, we use the hydrodynamic accretion disk wind simulations presented by PK04. The hydrodynamical simulations assume a $10^8$ M$_\odot$ black hole accreting at 1.8 M$_\odot$ yr$^{-1}$. These parameters correspond to an accretion rate of $0.5\ \dot{M}_{\rm Edd}$ assuming a radiative efficiency of 6 per cent. The gas is assumed to accrete through an optically thick, geometrically thin standard disk. The disk thermal uv radiation drives the wind. The simulations also include Comptonized continuum radiation from a central source which represents the emission from the inner parts of the accretion disk that are not covered by the computational domain. This component is not included in the line-driving calculation for the wind, because in the X-ray band there are relatively few line transitions. However, the central X-ray component has a major effect on the derived photoionization state. The properties of the outflow are calculated over the radial range 60 – 3000 $r_g$ (where $r_g = GM_{\rm bh}/c^2$ is the gravitational radius of the black hole).

To solve the equations of gas dynamics, PK04 used the ZEUS code which has been tested extensively (Stone & Norman 1992). Their version of the code has been modified to implement the radiation force, and radiative heating and cooling. PK04 approximated the radiative acceleration due to lines using a modification of the method developed by Castor et al. (1975). The radiative driving due to line scattering is treated using the generalized Sobolev approximation. This assumes the transport in the line core is dominated by the local velocity gradient. The coupling between the dynamics and

the radiation field is provided by radiation pressure and by thermal pressure due to radiative heating. The radiation pressure depends on the gas opacity, which in turn depends on the ionization balance. The effects of X-ray ionization on the radiation force due to lines is calculated using the procedure outlined by Stevens & Kallman (1990). In this procedure, the "force multiplier" of Castor et al. (1975) (the ratio of the full radiation force to that due solely to electron scattering) is suppressed by a factor which depends on the ionization parameter and temperature. The effects of heating by radiation are also taken into account by these calculations. Specifically, PK04 calculated the gas temperature assuming that the gas is optically thin to its own cooling radiation. Thus the net cooling rate depends on the density, the temperature, the ionization parameter, and the characteristic temperature of the X-ray radiation. In this case it is possible to fit analytical formulae to the heating and cooling rate obtained from detailed photoionization calculations for various gas parameters. PK04 used a fit to photoionization calculations obtained by Blondin (1994) who included Compton heating/cooling, X-ray photoionization heating/recombination cooling, bremsstrahlung and line cooling.

### 2.2 Monte Carlo radiative transfer simulations

The hydrodynamical simulations described above provide the time-dependent density and velocity structure of the disk wind. To compute synthetic spectra from these, we have performed radiative transfer simulations using the Monte Carlo code described in Papers I and II.

For the radiative transfer simulations, the Monte Carlo code was modified to accept a generalized axisymmetric wind with density and velocity specified via input data. As for the parametrized wind models adopted in Papers I and II, these input data define a 2D grid of wind properties (in this case, with properties depending on polar coordinates $r$ and $\theta$). The mass density in each wind grid cell is assumed to be uniform and taken from the hydrodynamical model. The three components of velocity ($v_r$, $v_\theta$ and $v_\phi$) at every point in the wind are obtained by linear interpolation (in $r$ and $\theta$) between the values which are provided at the boundaries of each wind grid cell. This interpolation is necessary since use of the Sobolev approximation for line transitions requires that the velocity is everywhere a smooth function.

In certain regions, particularly close to the disk plane where the transition between the disk atmosphere and the outflow lies, the hydrodynamical simulations predict rather high densities. In some cases, this makes certain grid cells very optically thick. Physically, any X-ray photons which penetrate deep within these optically thick layers will be thermalized and contribute to heating of the disk atmosphere. In the parametrized models considered in Paper II, this sink of X-ray photons was roughly accounted for by assuming that all Monte Carlo quanta which reach the $xy$-plane in the simulation strike the optically thick disk and are then lost. That approach neglects reflection by the disk but avoids the need to track the Monte Carlo quanta as they propagate through very optically thick material. In the more realistic model considered here, however, there is no sharply-defined boundary between the disk atmosphere and the wind. Thus reflection by the dense material at the very base of the outflow is automatically included in the simulations. However, this introduces additional computational challenges. In particular, quanta occasionally propagate deep into the optically thick regions where they interact many times and have very low probability of reemerging without being thermalized (and therefore lost to the X-ray regime since the expected temperature of the disk atmosphere is relatively low). To deal with these quanta, a cut is introduced whereby the flight paths of Monte Carlo quanta which propagate sufficiently deep into the base of the wind are terminated and it is assumed that these quanta contribute nothing further to the X-ray spectra or ionization state of the wind. A very conservative cut has been applied in the simulations presented here: quanta are terminated if they penetrate deep enough into the base of the wind that the Compton optical depth to re-emerge from the wind is greater than twenty in all directions.

As described in Paper II, the ionization and thermal structure of the wind are determined iteratively from the radiation field properties and the assumptions of ionization and thermal equilibrium. The ionization balance accounts for photoionization (including K-/L-shell ionization followed by ejection of Auger electrons), collisional ionization, radiative recombination and di-electronic recombination. Heating by photoionization, Compton down-scattering of X-ray photons and free-free absorption are balanced against bremsstrahlung, Compton cooling by low energy disk photons, bound-free recombination, bound-bound line transitions and cooling due to adiabatic expansion to estimate the local temperature. Note that our treatment of Compton cooling remains particularly approximate since we do not simulate the transport of the accretion disk photons in detail (see Paper II). The assumptions of ionization/thermal equilibrium are not perfectly valid in regions of the wind where the density is sufficiently low that the recombination/cooling timescales are long compared to the flow timescale. However, it alleviates the need to introduce explicit time-dependence in the calculation – a major computational saving. In general, we would expect that the most important consequence of departures from equilibrium is that the ionization state becomes frozen-in in the outer, low-density flow regions since recombination may become too slow to maintain local ionization equilibrium. As we shall show below, however, the equilibrium assumption already leads to near fully-ionized conditions in much of the outer wind – thus accounting for any further effective reduction to the recombination rate is unlikely to dramatically alter the typical ionization state.

The radiative transfer simulations were performed using the same set of atomic data as described in Paper II. This includes the K-shell ions of the astrophysically abundant metals, the L-shell ions of the important second and third row elements and the highest few M-shell ions of Fe and Ni. Note that this data set does not include M-shell ions of iron below Fe X – thus when the computed ionization state favours this ion it is likely that the true degree of ionization is lower. Similarly, a lower limit of $\log T_e[\mathrm{K}] = 4.0$ is imposed in the radiative transfer simulations since (i) the atomic data used is likely inadequate to describe the cooling to lower temperatures and (ii) the uv radiation of the disk – which is neglected here – should prevent the inner regions of the outflow from dropping to significantly lower temperatures.

### 2.3 Simulation parameters

The relevant physical and numerical parameters adopted in the simulations are given in Table 1. Most of these are carried over or derived from the parameters adopted in the radiation hydrodynamics simulation (Proga et al. 2000, PK04). For this study we have selected two snapshots of the wind structure; specifically we chose the wind conditions from timesteps 800 and 955 from the PK04 simulation. These timesteps were chosen since they are well-separated in simulation time (timestep 955 is later than timestep 800 by $\Delta t \sim 5$ years). This allows us to study two independent

**Table 1.** Parameters for the simulation.

| Parameter | Value |
|---|---|
| mass of central object, $M_{\rm bh}$ | $10^8$ M$_\odot$ |
| source luminosity, $L_{\rm bol}$ | $6.5 \times 10^{45}$ ergs s$^{-1}$ ($\sim 0.5 L_{\rm Edd}$) |
| X-ray source luminosity (2 – 10 keV), $L_X$ | $2.7 \times 10^{44}$ ergs s$^{-1}$ ($\sim 0.02 L_{\rm Edd}$) |
| source power-law photon index, $\Gamma$ | 2.1 |
| range of source photon energies in simulation | 0.1 – 511 keV |
| size of primary emission region, $r_{er}$ | $6r_g = 8.8 \times 10^{13}$ cm |
| inner radius of disk,$r_d$ | $6r_g = 8.8 \times 10^{13}$ cm |
| inner radius of simulated wind region, $r_{\rm min}$ | 60 $r_g = 8.8 \times 10^{13}$ cm |
| outer radius of simulated wind region, $r_{\rm max}$ | 3000 $r_g = 2.6 \times 10^{16}$ cm |
| outer radius of Monte Carlo Rad. Trans. simulation grid | $5 \times 10^{16}$ cm |
| 3D Cartesian Rad. Trans. grid cells | $256 \times 256 \times 256$ |
| 2D radiation-hydrodynamics polar grid zones | $100 \times 140$ |

realizations of the flow pattern and investigate how the spectral features should vary on timescales comparable to the typical interval between repeat observations of well-known AGN. Both snapshots show the characteristic structure of the PK04 simulation mentioned in Section 1 (a hot polar flow, warm rapid outflow, cold equatorial flow and a "failed wind" region). The relative importance of these structures is slightly different between the two-snapshots, however: this can be seen in the upper right panels of Figure 1 (mass density of the two-snapshots) and in Figure 2, which compares the hydrogen column densities for the two snapshots for different inclination angles, $\theta$ (measured relative to the rotation (z-)axis.)

For our radiative transfer simulations we need to fully specify the X-ray source radiation. We assumed that the radial extent of the primary emitting region is comparable to the size of the innermost stable orbit around a Schwarzschild black hole ($r_{em} = 6r_g$) and we also assumed that a geometrically thin/optically thick accretion disk lies in the mid-plane of the simulation, extending from an inner radius of $r_d = 6r_g$ to the outer boundary of the simulation grid. The X-ray source is assumed to radiate isotropically.

We assume that the primary X-ray radiation source is a pure power-law across the photon energy interval we simulate ($0.1 < h\nu < 511$ keV; see Paper II). We have adopted a photon index of $\Gamma = 2.1$. This is reasonably typical for the class of objects for which disk winds have been discussed as a possible site for the formation of X-ray spectral features (e.g. $\Gamma \sim 1.8$ for PG1211+143 [Pounds et al. 2003], $\Gamma \sim 2.4$ for Markarian 766 [Miller et al. 2007] or $\Gamma \sim 2.2$ for MCG-6-30-15 [Miller et al. 2008]). To estimate the appropriate normalisation of the primary power-law X-ray emission, we used the source X-ray luminosity of 0.05 $L_{\rm Edd}$ adopted by PK04. The role of the X-ray luminosity in the radiation hydrodynamics simulation is to estimate the ionization parameter required to compute the line driving force multiplier. PK04 used the relationship between force multiplier and ionization parameter derived by Stevens & Kallman (1990) which was based on calculations assuming a bremsstrahlung source spectrum with temperature $T_X = 10$ keV. Therefore, we fixed the normalisation of our input X-ray luminosity spectrum ($L(E) \propto E^{-\Gamma+1}$) to give the same total X-ray flux (integrated from 1 to 20 keV) as for a bremsstrahlung spectrum ($L(E) = 0.05 L_{\rm Edd} \exp(-E/T_X)/kT_X$). This yields a 2 – 10 keV luminosity of $L_X = 0.02 L_{\rm Edd}$ which is comparable to the observationally motivated estimates for $L_X/L_{\rm Edd}$ adopted for the models described in Paper II.

The Monte Carlo code requires that the total photon luminosity ($L_{\rm bol}$) be specified in order to estimate the role of Compton cooling in the wind (see Paper II). We have adopted $L_{\rm bol} = 6.5 \times 10^{45}$ ergs s$^{-1}$ ($= 0.5 L_{\rm Edd}$) which is consistent with the accretion rate ($0.5 \dot{M}_{\rm Edd}$) and radiative efficiency ($\eta = 0.06$) adopted by PK04.

## 3 RESULTS

As described in Paper II, the ionization state and kinetic temperature in the wind are computed from the radiation field properties via an iterative sequence of Monte Carlo simulations. We will first describe the results of this part of the calculation and then present the synthetic spectra.

### 3.1 Temperature structure

Figure 1 shows the temperature distribution computed from the Monte Carlo radiative transfer simulations for the two snapshots (top and second row, left panels). In both cases the temperature structure is complex but can be easily understood as a consequence of the density distributions (top and second row, right panels in Figure 1) and the central location of the primary X-ray source. The low-density polar wind cone is strongly irradiated by the X-ray source and is therefore both hot and very highly ionized (see Figure 3, discussed below). Below this region lies a warm stream ($T_e \sim 10^6$ K) where the relatively dense portions of the wind are exposed to the primary X-rays. Deeper inside, the wind becomes significantly cooler, down to $T_e \lesssim 2 \times 10^5$ K in the outer regions. The densest material (comprising the "failed wind" region and the atmosphere of the outer parts of the disk) is not significantly heated by the X-ray source and remain at the lower temperature boundary imposed in the simulations ($T_e = 10^4$ K).

The computed temperature (and ionization) structure of the disk wind are noticeably different from those obtained in the original hydrodynamical simulations of PK04. For comparison, the temperature distribution for the timestep 955 snapshot obtained from those simulations is also shown in Figure 1 (bottom left panel). There are several qualitative differences: most importantly, the dense regions of the outflowing gas are significantly cooler that obtained here. This can be attributed to the differences in the radiative transfer schemes employed. In particular, PK04 did not include scattering – they assumed that the wind is a pure absorbing structure. Our Monte Carlo method is considerably more sophisticated and includes both scattering and true absorption. To illustrate the

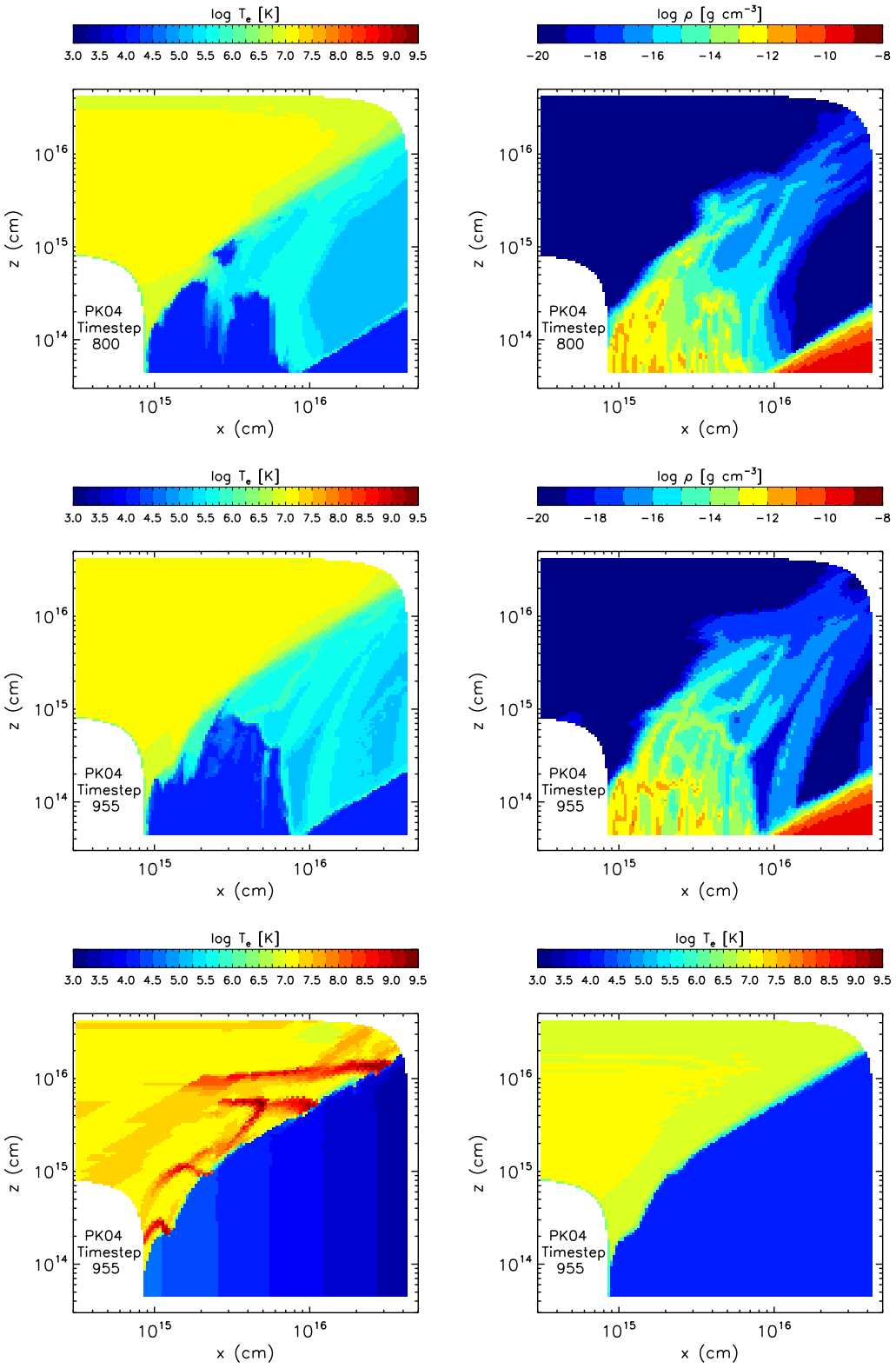


**Figure 1.** Distribution of kinetic temperature ($T_e$) computed from our Monte Carlo radiative transfer simulations (top/middle left) and mass density (top/middle right) for the two snapshots we consider from the PK04 simulation (timesteps 800 and 955; top and middle rows, respectively. For comparison, we also show the temperature obtained for timestep 955 in the PK04 radiation-hydrodynamics simulations (lower left). The lower right panel shows the temperature distribution obtained with our Monte Carlo code (for the timestep 955 snapshot) when heating by scattered/reprocessed radiation is neglected. Note the logarithmic axes. The figures show the complete computational domain of the hydrodynamical simulation ($60r_g < r < 3000r_g$). A lower temperature limit of $T_e = 10^4$ K was imposed in the Monte Carlo radiative transfer simulations.

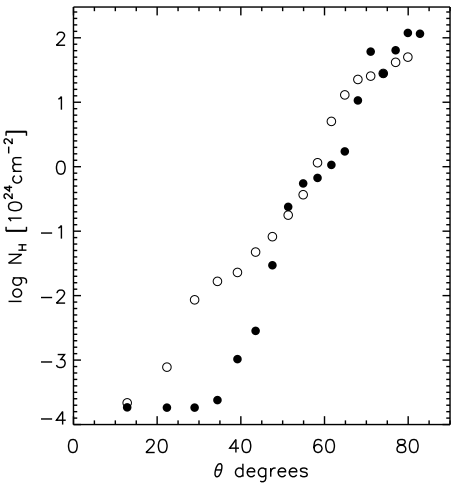


**Figure 2.** Hydrogen column density, $N_H$ versus inclination angle $\theta$ (measured relative to the rotation (z)-axis) for the two snapshots from the PK04 simulation for which we compute spectra (filled circles for timestep 800, open circles for timestep 955).

importance of this, we also computed the temperature distribution if only the heating due to direct irradiation is considered for the same snapshot (i.e. heating by radiation which is either scattered or reprocessed in the wind is neglected; see bottom right panel in Figure 1). This reproduces the low temperatures found in the entire region shielded by the "failed wind" in the radiation hydrodynamics simulation. Thus our Monte Carlo simulations show that scattered/reprocessed X-ray radiation can be rather important in determining the physical conditions in the disk wind, particularly for material that is shielded from direct radiation by the X-ray source.

There are several other, relatively inconsequential, differences between the temperature distribution obtained from the Monte Carlo radiative transfer simulations and the radiation hydrodynamics. The polar wind is generally found to be hotter with the radiation hydrodynamics code than the Monte Carlo code. This is partly a consequence of the different forms of the adopted X-ray spectrum. In both codes, much of this material is predicted to be close to the Compton temperature $T_c$ but PK04 adopted an X-ray temperature of 10 keV (yielding $T_c \sim 3 \times 10^7$ K) while the input spectrum of the Monte Carlo simulation (power-law X-ray spectrum combined with total luminosity $L_{\rm bol}$) gives a lower value of $T_c \sim 10^7$ K. Also, in the radiation hydrodynamics calculation, the region above the dense disk wind contains structured regions in which the temperature is much higher due to shock heating (interactions between expanding and falling parts of the flow). Since non-radiative heating is not included in our Monte Carlo code, such high temperatures are not found in our radiative transfer simulations. We note, however, that the exactly physical conditions in these polar regions are rather unimportant for the spectrum since this material is generally optically thin. Thus the consequences of any discrepancy between the radiation-hydrodynamics and Monte Carlo radiative transfer simulations in the low-density polar regions are relatively minor.

### 3.2 Ionization conditions and Fe K$\alpha$ forming regions

Since the X-rays are responsible for both ionization and heating in our Monte Carlo simulations, the distribution of ionization state in the wind is qualitatively similar to the temperature distribution. This is illustrated in Figure 3 which shows the distribution of mean iron ionization state computed for both snapshots. In the low density polar regions the material is almost fully ionized whilst the denser streams in the flow are less ionized. Only the dense outer regions of the disk atmosphere (large radial coordinate) and the "failed wind" region are not significantly ionized.

A noteworthy convenience of the Monte Carlo method is that, by analyzing the flight paths of quanta, it is relatively easy to identify which parts of the outflow are responsible for the formation of particular spectral features. Since much of the discussion below will be devoted to the Fe K region, we have examined the Monte Carlo quanta which contribute to this part of the spectrum in detail. Specifically, since the Monte Carlo simulation follows the complete flight paths of the quanta, we can flag each quantum to identify which physical processes (e.g. bound-bound transition, Compton scattering etc.) were responsible for determining its properties (e.g. photon energy, direction of emission etc.) as it left the computational domain. To understand the formation of the Fe K band spectra, we identified all escaping quanta whose last physical interaction (excluding Compton scattering) resulted in line emission via an Fe K$\alpha$ transition. These packets are responsible for Fe K$\alpha$ emission features in the spectrum. We then binned these quanta based on the position of the Fe K$\alpha$ emission which gave rise to them. The resulting distribution, which is shown for the PK04 timestep 800 snapshot in Figure 4, indicates which portions of the flow are responsible for the creation of the Fe K$\alpha$ emission features. Since the emission line profile can be affected by Compton scattering, we also recorded the positions of the final Compton scattering event for the quanta flagged as contributing to the Fe K$\alpha$ emission. These allow us to identify the parts of the model in which scattering of the Fe K$\alpha$ emission takes place – this region is also indicated in Figure 4. Note that the plot does not retain any information related to observer orientation – all escaping Monte Carlo quanta are included, independent of their direction of propagation.

Much of the Fe K$\alpha$ line formation is concentrated in the inner parts of the flow structure: roughly 50 per cent of the escaping Fe K$\alpha$ photons are created within a radial extent of $r \lesssim 2 \times 10^{15}$ cm while $\sim 90$ per cent are formed inside $r \lesssim 7 \times 10^{15}$ cm. Comparing Figure 4 to Figures 1 and 3, it is apparent that the most intense region of Fe K$\alpha$ formation is around the inner surface of the "failed wind". This is expected since it is here that the X-ray radiation from the central source most directly strikes relatively dense material from which it can be reflected. K$\alpha$ formation continues throughout most of the moderate density outflowing region outside the "failed wind", however, and there is also a reflection component formed from the dense material near the disk atmosphere (equatorial regions) at large radii. Shielding by the "failed wind" means that this region is not directly irradiated by the central source but reflection still occurs thanks to illumination by X-rays scattered in the upper portions of the wind.

In the outer wind, there are regions where the ionization state is too high for significant numbers of Fe K$\alpha$ photons to be produced but where Compton scattering of K$\alpha$ photons created deeper in the wind can still occur. Regions such as this are potentially critical since Compton scattering in a fast outflow may have a role in shaping emission line profiles (see e.g. Laurent & Titarchuk 2007). In our simulations, escaping Fe K$\alpha$ photon packets undergo an average of about two Compton scatterings between their creation and escape ($\sim 40$ per cent escape with no Compton scattering while $\sim 15$ per cent undergo five or more Compton scattering events).

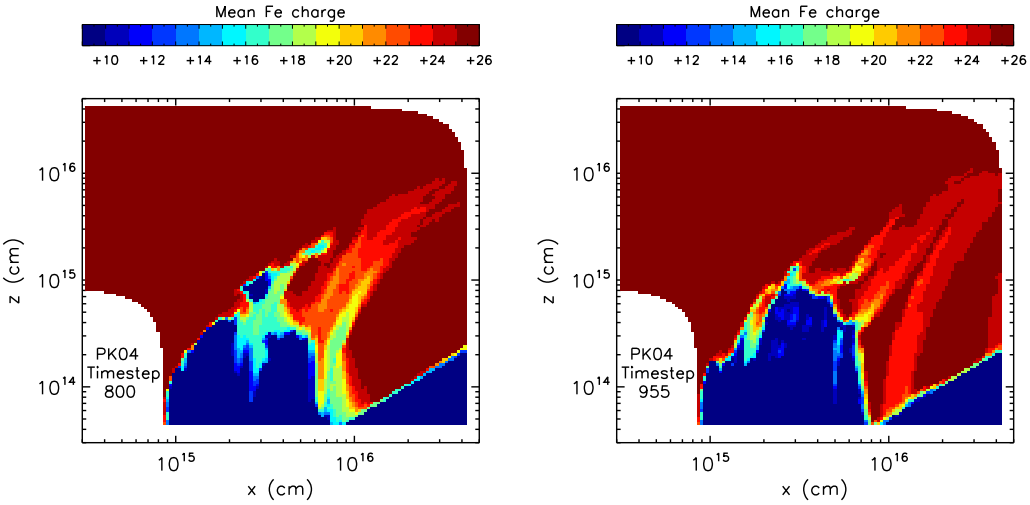


**Figure 3.** The distribution of mean Fe ionization state for the two snapshots obtained from the Monte Carlo code (timesteps 800 and 955 from PK04; left and right, respectively). Since we do not include ionization stages of iron below Fe X, the computed ionization state in the dark blue areas is only an upper limit on the degree of ionization.

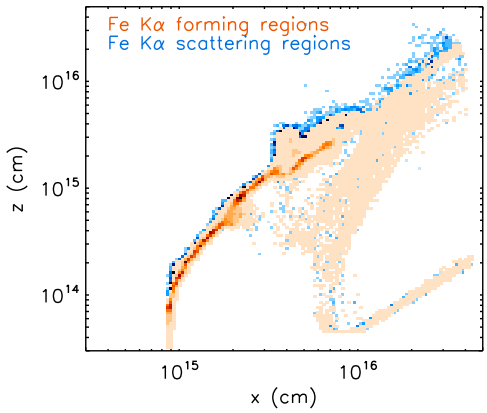


**Figure 4.** Regions responsible for the creation and subsequent scattering of the Fe K$\alpha$ photons which contribute to the spectra for the snapshot from timestep 800 of the PK04 simulation. Each grid cell is shaded orange/red if Monte Carlo quanta representing Fe K$\alpha$ photons were created in that cell and subsequently escaped without undergoing any further physical interactions (except Compton scattering). The intensity of the shading is proportional to the Fe K$\alpha$ luminosity of the cell (ergs s$^{-1}$; i.e. the volumes of the cells are not taken into account). Grid cells are shaded blue if no Monte Carlo quanta representing Fe K$\alpha$ photons were created in that cell but Compton scattering of escaping Fe K$\alpha$ photons did occur there. White regions indicate that either no Fe K$\alpha$ photons were created/scattered there or that any such photons were subsequently destroyed and so did not contribute to the spectra.

### 3.3 X-ray spectra

#### *3.3.1 General characteristics*

Given the complex structure of the outflow (see Figure 1) and the high column densities for many lines-of-sight (see Figure 2) the emergent spectrum is expected to be strongly dependent on the observer inclination angle ($\theta = \cos^{-1}\mu$). As in Paper II, we extracted spectra for twenty different observer orientations, uniformly sampling the interval $1 > \mu > 0$. Figure 5 shows the spectra computed for three example observer orientations for the snapshot from timestep 800 of the PK04 simulation. Despite the underlying complexity of the wind model, these spectra are qualitatively rather similar to those obtained from the simply-parameterized smooth wind models used in Paper II. The spectra can be broadly classified into three groups, differentiated by the observer orientation; these are exemplified by the spectra shown in Figure 5 and discussed below.

For relatively pole-on inclinations (first panel of Figure 5), the direct component of radiation is largely unattenuated and supplemented by reflected radiation from the wind. As described in Section 3.2 (see Figure 4), the most intense reflection occurs at the inner irradiated surface of the wind (the "failed wind" region) and this gives rise to a reflection component when observed pole on. Qualitatively similar to reflection contributions in the parametrized disk wind models used in Paper II and disk reflection models (Ross & Fabian 2005), this reflection component introduces both line emission and a Compton hump to the spectrum. The emission line features are moderately strong (the Fe K$\alpha$ line has equivalent width, EW $\sim$ 140 eV for the upper spectrum in Figure 4) and significantly broadened by the Doppler motions of the material (full-width at half-maximum, FWHM $\sim$ 700 eV, determined by Gaussian fitting). In addition, Compton scattering of reflection line photons in the outflow causes weak, red-skewed line wings to develop. This can be seen in the right-panels of Figure 5 which show details of the spectrum around the strong Fe K$\alpha$ line.

For moderate inclination angels (second row of Figure 5), the primary X-ray source is obscured by the high-ionization, fast outflow component. For these orientations, Compton scattering is the dominant opacity source along the line-of-sight although absorption lines associated with high ionization state material (most clearly, Fe XXVI Ly$\alpha$) are also imprinted on the transmitted spectrum. These features are generally rather narrow but blueshifted from their rest energies due to the net outflow along the line of sight. Emission features, typically slightly broader (FWHM

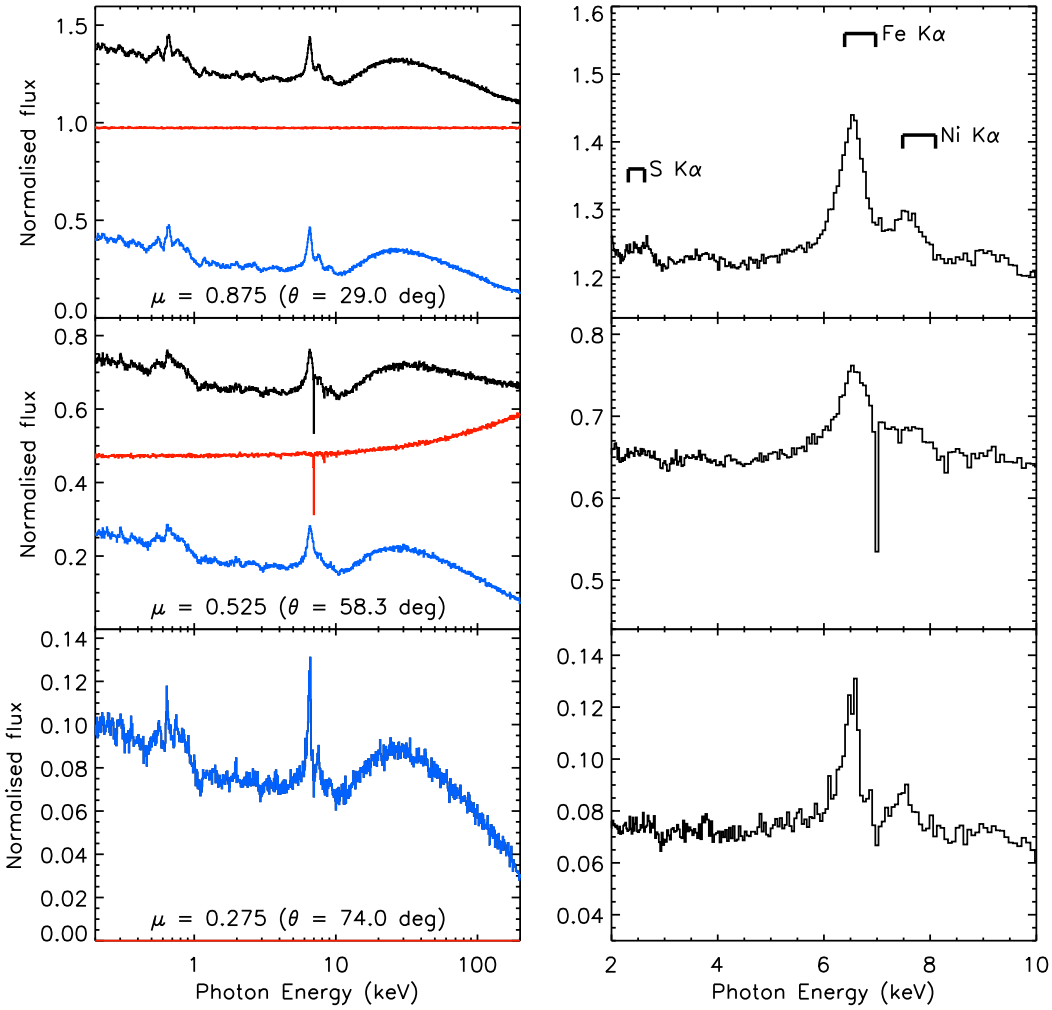


**Figure 5.** Spectra computed for three observer orientations (specified by $\mu = \cos^{-1}\theta$ where $\theta$ is the inclination of the observer measured from the z-axis) for timestep 800 of the PK04 simulation. The left panels show the photon energy range 0.2 – 200 keV while the right panels show the 2 – 10 keV region (including the Fe K$\alpha$ line) in detail. In the left panels, the total spectrum (black) is subdivided into contributions from photons which have come directly from the primary X-ray source (red) and photons which arise from scattering/reprocessing in the outflow (blue). All spectra are normalized to the input primary X-ray spectrum (which was a pure power-law with photon index $\Gamma = 2.1$). The range of rest-energies for Fe, Ni and S K$\alpha$ transitions (6.4 – 6.97 keV, 7.5 – 8.1 keV and 2.3 – 2.6 keV, respectively) are indicated in the upper right panel.

$\sim$ 800 eV) and with somewhat more developed red wings than predicted for polar inclinations, are also moderately strong for these orientations.

At higher inclination, the absorbing column density is larger and the direct component of the spectrum becomes increasingly dominated by the scattered/reprocessed component (third panel of Figure 5). This results in a spectrum with prominent emission lines (Fe K$\alpha$ EW $\sim$ 400 eV) and a stronger Compton hump.

In most respects, the spectra we obtain from the two snapshots lead to qualitatively similar conclusions: in particular, the same characteristic spectra features (Compton hump, Fe K$\alpha$ emission line, blended emission lines at soft energy, blue-shifted absorption lines) manifest and have similar dependence on the observer inclination. For fixed orientation, the emission features also have comparable strength in the two snapshots, being just slightly stronger (typically by $\sim$ 30 per cent in flux) in the second snapshot (recall that the second snapshot has typically higher column densities which makes scattered/reprocessed radiation more dominant). In detail, however, there are some interesting quantitative difference between the absorption line properties of the two snapshots, mostly for intermediate observer orientations, which we will now discuss in greater detail.

### 3.3.2 *Complexity at intermediate orientations*

In both snapshots, the dependence of the spectrum on inclination angle is relatively modest when the orientation is either high or low. The sensitivity is strongest for intermediate orientations, mostly because of the rapid change in the transmission properties of the wind for inclinations that pass through the complex outflowing structure. It is in this range of orientation angles that the most complex spectra occur but also where the least ambiguous outflow signatures (e.g. narrow, blueshifted absorption lines – see Paper I) can manifest. To map out the spectra in this sensitive regime, we repeated

the Monte Carlo simulations extracting spectra for a finely spaced grid of twenty inclination angles (with $\Delta\theta = 1$ deg) centred around the orientation used in the second panel of Figure 5 (48 deg $< \theta <$ 67 deg). A subset of the spectra obtained for this set of inclination angles in the timestep 800 snapshot is shown in Figure 6, divided into the component of radiation reaching the observer directly from the X-ray source and that formed by scattering/reprocessing in the disk wind structure.

As expected, the direct component of the spectrum (upper panel in Figure 6) is a stronger function of inclination than the scattered/reprocessed component. This can be readily understood since the scattered/reprocessed spectrum is formed by an integration over all positions in the flow and is therefore relatively insensitive to a small ($\sim$ 1 deg) change in inclination. In contrast, the attenuation of the direct component is determined only by the conditions in the narrow column of gas which obscures the small (assumed $r_{em} = 6r_g$) X-ray emission region. Since the properties of the line-of-sight column change rapidly with inclination, this component of the spectrum is strongly dependent on $\theta$. Our calculations for the direct component of the radiation field are in qualitative agreement with the results of Schurch et al. (2009): they demonstrated that strongly orientation-dependent attenuation is expected in the PK04 simulation for $50$ deg $\lesssim \theta \lesssim 67$ deg (see e.g. their figure 1)[1]. But since their calculations effectively include *only* the direct component of the radiation field, we argue that their study overestimates the role of absorption in shaping the X-ray spectrum: in our emergent spectra (composed of the the sum of the two components shown in Figure 6), scattered/reprocessed light dominates for many inclinations leading to spectra with less dramatic absorption features and overall weaker dependence on the observer orientation.

The full spectra (direct plus scattered) around the Fe K$\alpha$ region for intermediate inclination angles are shown for both of our snapshots in Figure 7. This illustrates the most striking difference between the spectra obtained from the two snapshots, namely the behaviour of the blueshifted absorption lines. Owing to the fairly narrow range of polar angles at which a fast wind is present in the model, it is only for a modest fraction of lines-of-sight that clean, sharp absorption lines appear in our computed spectra for either snapshot. In the timestep 800 snapshot, an Fe K$\alpha$ absorption line is present for a range of inclinations $\Delta\theta \sim 12$ deg. For the later snapshot, the range is even smaller, $\Delta\theta \sim 5$ deg. In our previous work (Papers I and II), narrow absorption lines also only appeared for only a minority of inclinations although they were generally more common than found here. This is likely a consequence of the simplicity of the velocity law adopted in the parametrized models (Papers I and II) – by adopting a smooth outflow velocity at all points, those models increase the fraction of lines-of-sight which pass through moderately opaque material with a significant component of velocity directed towards the observer. In contrast, the model considered here has a much more complex velocity field leading to a rarer occurrence of clean outflow signatures.

Most importantly, the blueshifted absorption features are dramatically different between the two snapshots. In the timestep 800 snapshot, the Fe K$\alpha$ absorption line not only manifests for a wider range of inclinations but it is generally significantly sharper, deeper and *less* blueshifted compared to the same inclination in the timestep 955 snapshot. The maximum Fe K$\alpha$ blueshift for the first snapshot corresponds to only $\sim 0.015$c while it is as large as $\sim 0.06$c for the later snapshot. The largest Fe K$\alpha$ absorption EW is similar in both snapshots $\sim 70$ eV, although this occurs for different $\theta$-values ($\theta \sim 66$ deg for timestep 800 and $\theta \sim 60$ deg for timestep 955). For fixed inclination angle, the absorption EW changes quite significantly (a factor of two or more) between the two snapshots for most orientations. Thus the model predicts that the properties of blueshifted absorption features should not only be a strong function of observer orientation but will also be significantly variable on timescales comparable to the time difference between our snapshots ($\Delta t \sim 5$ years). We note that the calculated continuum level is also different between the two snapshots, most obviously around $\theta \lesssim 65$ deg. This is attributable to the larger column densities for these lines-of-sight in the timestep 955 snapshot (see Figure 2).

In contrast, the model predicts that emission features (in particular, Fe K$\alpha$) should be present in the spectrum for all observer orientations and that their character will be less dramatically time-variable (except for $\theta > 75$ deg, the Fe K$\alpha$ emission flux typically changes by no more than $\sim 30$ per cent between the two snapshots). The relative insensitivity of the emission line flux arises from the fact that they are formed over an extended region in the flow and are thus less affected by details of the structure along the observer's line of sight. As noted above, it is at the same inclination angles for which absorption line features form that the emission lines are most intrinsically broad (FWHM $\sim 0.8$ keV) and also where they develop the most noticeably red-skewed wings via Compton scattering in the flow (see Figure 8). We note that the red line wings found in the current simulations are somewhat less well-developed than in the simplified models considered in Papers I and II; this is expected since the fast wind component, in which Doppler shifts can most effectively give rise to the red-skewed wing, occupies only a relatively small region of the model.

## 4 SUMMARY, DISCUSSION AND CONCLUSIONS

We have applied our Monte Carlo radiative transfer code (see Papers I and II) to compute X-ray spectra for snapshots from a radiation-hydrodynamics simulation of a line-driven AGN disk wind (PK04). In most important respects, we find that the results of these simulations support conclusions drawn from our previous studies of parametrized outflow models. In particular, (1) we find that a disk wind should imprint a wide range of spectroscopic features in the X-ray band and (2) the role of the wind in reflecting/scattering/reprocessing radiation in these simulations is *at least* as important as the part it plays in imprinting absorption signatures.

Since we have considered only two snapshots from one model, one should not expect that the simulated spectra will quantitatively match observations. Rather the synthetic spectral features should be interpreted as broadly indicative of those which a disk wind may cause. This should guide future studies in which the hydrodynamical modelling will be improved and the system parameters explored. It should also be borne in mind that the PK04 simulation was primarily an attempt to build insight to the problem of line-driven AGN winds and is not expected to capture all the detailed physics. In particular, since the model is axisymmetric, it will not correctly describe any small scale clumping in the flow.

In the following sub-sections we first discuss the relevance of our results to the interpretation of X-ray spectra (Section 4.1). We

[1] Note that perfect agreement between our calculation of the transmitted spectrum and those of Schurch et al. (2009) is not expected since our calculation includes the effects of ionization by scattered light and we have adopted a different spectral shape for the source of ionizing radiation. In general, we obtain a higher ionization state of the absorbing gas for intermediate inclination angles than they found.

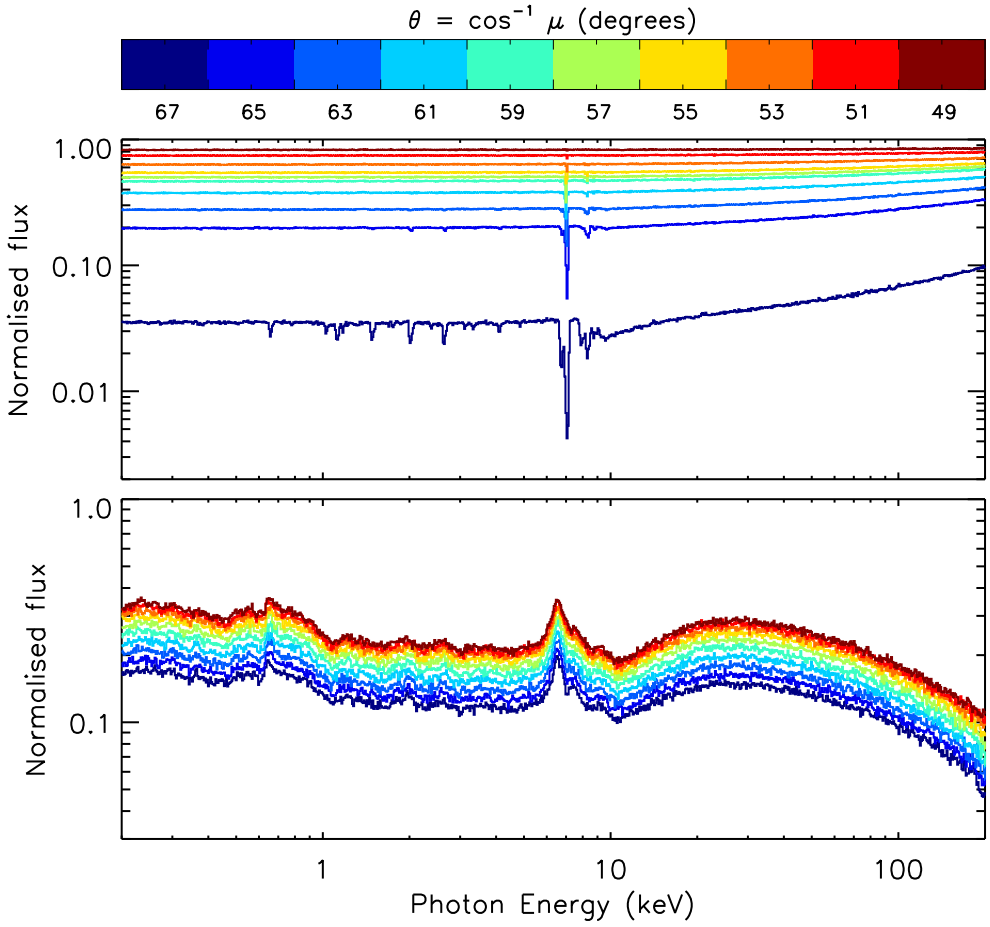


**Figure 6.** Direct (upper) and scattered/reprocessed (lower) components of the spectrum computed for 48 deg $< \theta <$ 67 deg for timestep 800 of the PK04 simulation (each inclination is indicated by a different colour; see colour bar in figure). The complete model spectrum (see Figure 7, left) is composed of the sum of these two components. Note the different ordinate scale used in the two panels. All spectra are normalized to the input primary X-ray spectrum (which was a pure power-law with photon index $\Gamma = 2.1$).

then comment on the comparison of our spectra to those obtained from the parametrized models used in Papers I and II (Section 4.2) before discussing the implications of our work for the modelling of line-driven winds (Section 4.3) and, finally, highlighting some of the outstanding questions in Section 4.4.

### 4.1 Implications for the interpretation of X-ray spectra

#### *4.1.1 Absorption lines*

Our first application of a Monte Carlo code to the modelling of the X-ray spectra of AGN (Sim 2005) was motivated by the identification of narrow, blueshifted absorption lines in the Fe K band (e.g. Pounds et al. 2003). Such features are the least ambiguous signature of a fast, highly-ionized outflow. This study confirms that such features can arise in a plausible disk wind geometry. Our calculations suggest that narrow, blueshifted K$\alpha$ absorption lines will manifest in systems with line-driven disk winds for a limited range of orientations (very roughly $\Delta\theta \sim 2 - 10$ deg, centred around moderate inclination angles of $\theta \sim 57$ deg). For an isotropic distribution of observed orientations, this would suggest that only a modest fraction of sources (somewhere around $\sim 3 - 15$ per cent) should show any such absorption lines. The fraction in the observed sample of X-ray bright AGN would be expected to be somewhat higher since very high inclination systems are likely excluded – but it should still be a minority. Thus the absence of this "smoking gun" signature of outflow is not evidence against the presence of a fast wind and the calibration factor required to convert the fraction of objects with observed narrow line features to the fraction with powerful disk winds may be large.

Moreover, comparing the spectra obtained from the two timesteps we considered demonstrates the absorption line properties should be significantly variable on timescales comparable to $\Delta t \sim 5$ years. Thus, even if the flow is persistent, re-observations of particular objects are not expected to yield very similar absorption line properties over timescales of years: for a fixed observer orientation, the line blueshifts, widths and equivalent-widths can all change significantly. This is consistent with observations of e.g. PG1211+143, an object where blueshifted Fe K$\alpha$ absorption has been claimed but in which the absorption properties have varied between multiple observations made over the course of the last decade (see e.g. Pounds et al. 2003, 2005; Pounds & Reeves 2007, 2009). Our current radiative transfer simulations do not constrain

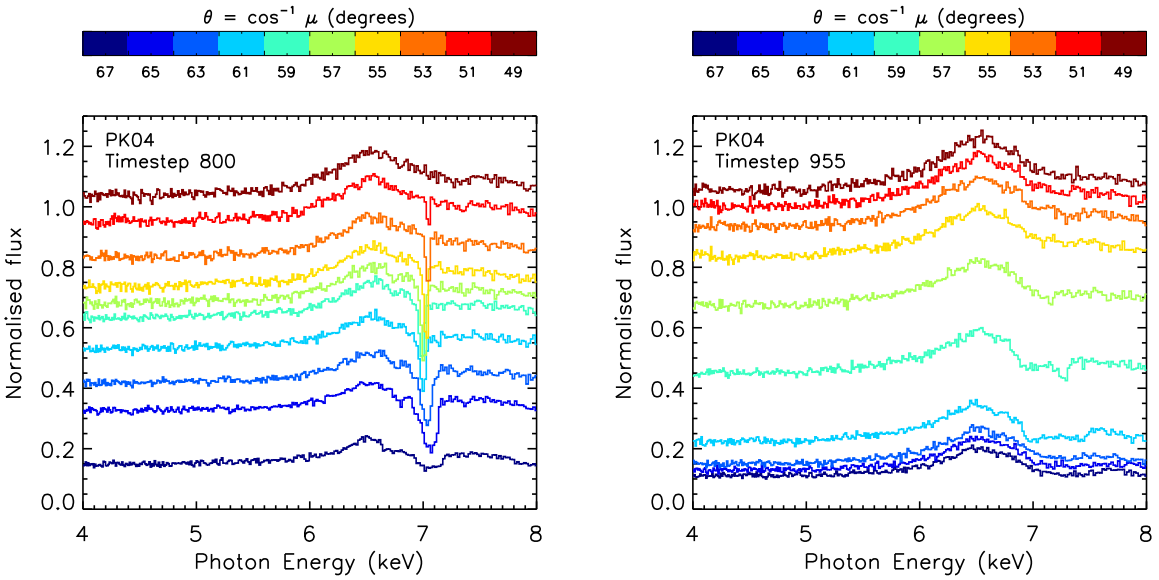


**Figure 7.** Spectra in the Fe K$\alpha$ region for 48 deg $< \theta <$ 67 deg (each inclination is indicated by a different colour) for the two snapshots (timestep 800 and 955; left and right respectively), which are separated by $\Delta t \sim 5$ years. All spectra are normalized to the input primary X-ray spectrum (which was a pure power-law with photon index $\Gamma = 2.1$. The small-scale fluctuations are due to Monte Carlo noise in the simulations.

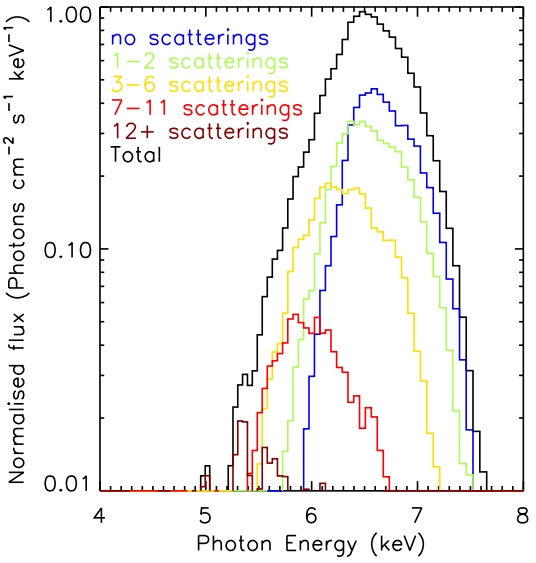


**Figure 8.** The spectrum of escaping Fe K$\alpha$ photons computed for an observer inclination around 55 degrees for the timestep 800 snapshot from the PK04 simulation. The solid black line shows the complete spectrum of escaping Monte Carlo packets whose last physical interaction, excluding Compton scattering, was with an Fe K$\alpha$ transition. The coloured lines show the subdivision of this profile into contributions from packets which underwent particular numbers of Compton scattering events after their interaction with an Fe K$\alpha$ transition. The spectra are normalized to the peak of the line and have been slightly smoothed to suppress Monte Carlo noise.

the level of absorption line variability expected on much shorter timescales (e.g. on the scale of typical X-ray exposures of several kiloseconds). Detailed consideration of shorter timescales will require a more extensive, tightly-spaced sequence of snapshots and investigation of the role played by both small-scale structure in the flow (which will not be well-represented in the axisymmetric simulation considered here) and intrinsic, short time-scale variability of the primary X-ray source. We would like to note, however, that (i) variations in the wind structure itself occur on a very wide range of timescales, at least as short as $\sim 10^5$s – thus we expect that some degree of variability will also be present on much shorter timescales than the time difference between the two snapshots used here; and (ii) short time-scale variability (timescales $\lesssim 10^5$ s) is much more likely to manifest in the absorption lines than any emission features since the light-crossing time for the simulation ($\sim 0.01$ yr $= 3 \times 10^5$ s) sets a lower limit for the timescale on which the emission from the outflow should show significant variability.

### 4.1.2 *Emission features*

Whilst narrow absorption features appear for only a limited range of observer orientations, other spectroscopic signatures associated with emission/reflection by the wind are predicted to appear for *all* inclination angles:

(i) A Compton hump is present for all observer inclinations. This generally causes the spectrum to smoothly rise across the energy interval $\sim 10 - 25$ keV. At harder energies it either flattens or, for high inclination angles, turns down. In the current simulation, the amplitude of the rise is quite modest, typically several tens per cent (measured relative to a power-law extrapolated from lower energies).

(ii) For all observer orientations, the 2 – 10 keV band shows a fairly broad Fe K$\alpha$ emission line (and corresponding, but weaker, Ni and S features). This feature is shaped by fluorescence, recombination and scattering around the surface of the dense "failed wind" region and in the fast outflow. It can be fairly strong (emission EWs of at least ∼150 eV for most orientations) and can develop a modest red-skewed wing due to Compton scattering of line photons in the outflow. Thus, for a realistic disk wind configuration, a signif-

icant component of strong, broad Fe K$\alpha$ emission with a complex line profile can be easily produced.

(iii) Below $\sim$ 1 keV an additional emission component forms from multiply blended line and continuum features. These are dominated by reflection/reprocessing by the abundant elements Fe, O and C and a modest component of bremsstrahlung emission from the wind. Most of the emission features are strongly blended although there is always a fairly prominent O emission feature at 0.7 keV and significant Fe emission at 0.8 keV. We note that, because it is often a complex blend, the exact strength and shape of this low energy emission will be sensitive to changes in the relative element abundances (which were fixed to their solar ratios here).

Qualitatively, each of the three classes of feature mentioned above is known from observations of AGN (hard band excesses, Fe K$\alpha$ emission, excess soft band emission; see e.g. Turner & Miller 2009). Given that there are many simplifying assumptions in the PK04 simulation and that we have made no attempt to tune the simulation parameters, we find it encouraging that such observable signatures are immediately predicted.

Although the EWs of our K$\alpha$ emission lines are comparable to those measured for the strongest narrow K$\alpha$ line components in AGN, our emission lines are too broad to account for these: Shu et al. (2010) typically find Fe K$\alpha$ line cores that have FWHM $< 10,000$ km s$^{-1}$ while our lines have FWHM $\sim 30,000$ km s$^{-1}$. The observed narrow line cores are therefore more likely to originate in structures further out than the main line-forming regions in our simulations. Our synthetic emission line profiles can be more realistically connected with moderately broadened line components such as reported in MCG-5-23-15 by Braito et al. (2007). For such a case, the agreement in FWHM of the profile is much closer although the emission EWs obtained from the current model are too large by a factor of a few. Although interesting, the amplitude of the rise in flux between $\sim$ 10 and 25 keV is small compared to that required to explain *Suzaku* observations of hard excesses in AGN (e.g. PDS 456 Reeves et al. 2009; NCG 4051 Terashima et al. 2009; 1H0419-577 Turner et al. 2009). To explain such strong excesses requires absorption by high column-density optically-thick clumps along the line of sight. To fully explore this possibility in disk wind models will require full three-dimensional simulations to be undertaken in the future (see Section 4.4).

We argue that the qualitative properties of the spectra obtained from the current model (with no tuning/exploration of parameter space) encourages further study of disk wind models. We are certainly forced to the strong conclusion that a line-driven disk wind should imprint several X-ray spectroscopic features in addition to "smoking gun" blueshifted absorption line features. Thus, if the fast outflows required to explain blueshifted absorption lines are associated with a disk wind, it seems inevitable that the outflow will also have an important part in shaping many other spectral features, even when it does not directly obscure the primary X-ray source region.

### 4.2 Comparison to parametrized models

All the classes of spectral feature described above appeared in our calculations with simply-parametrized outflow models (see figs. 3 and 4 of Paper II). Qualitatively, the features have comparable strengths and fairly similar shapes to those obtained with Model B in Paper II. The narrow absorption line features also have approximately the same maximum blueshifts. The most apparent quantitative difference is the relative paucity of narrow absorption features in the spectra computed here. Also, despite having a wind mass-loss rate ($\dot{M}_w$) which is a significantly smaller fraction of the Eddington accretion rate, the model presented here predicts emission features which are comparably strong to those in the parametrized models used in Paper II ($\dot{M}_w \sim 0.06\dot{M}_{\rm Edd}$ here but was $\gtrsim 0.6\dot{M}_{\rm Edd}$ in the models adopted in Paper II). Thus the effective emission measure of the hydrodynamical wind must be higher than that of the equivalent parametrized model with the same mass-loss rate. In addition, the red-skewed emission line wings are typically less well-developed than in the parametrized models.

These differences can all be attributed to the greater complexity of the hydrodynamical model: in contrast to the parametrized models, it is not a steady-state flow but has density and velocity variations that are not simple functions of azimuth and radius. Moreover, neither the "failed wind" region nor the dense material around the disk at large radii are captured in the parametrized model. Both these regions contribute to the Fe K$\alpha$ line emission (see Figure 4; i.e. these regions increase the effective emission measure of the wind).

We conclude, therefore, that the simply-parameterized models provide a good means by which to study the influence of a disk wind on the spectrum. In particular, such models provide a reasonable description of how a successfully launched outflowing component imprints blueshifted lines and associated broad emission features from highly ionized material. There is, however, an important and obvious caveat with parametric modelling, namely that it is only useful to the degree that it reflects the physical properties of the wind. In our case, the parametric model is a poor representation of the "failed wind" component, a component which does have an affect on the overall spectrum. One must always be cautious about quantitative results derived from a parametric wind description.

Taken together, our studies (Papers I, II and this work) suggest that models in which a smoothly outflowing component is dominant will predict relatively common blueshifted absorption features (and more strongly-developed red-skewed line wings) compared to a flow with complex topology. In particular, narrow blueshifted K$\alpha$ absorption is most likely to be clearly seen in flows with moderate covering fractions along lines-of-sight that have modest continuum optical depths (see discussion in Paper I). Relative to emission features, these absorption line features are likely to be rarer in scenarios in which other flow components (e.g. the "failed wind" in the simulation presented here) have significant covering fractions. Thus, there are good prospects that an unbiased census of X-ray absorption line features could, in the future, place constraints on the typical geometry required for wind models.

### 4.3 Implications for the theory of AGN winds

In this study, we have adopted the existing radiation-hydrodynamics simulation of PK04 and performed detailed radiative transfer simulations as a post-processing step, assuming that the underlying density/velocity distributions are appropriate. Our detailed X-ray radiative transfer calculations, however, point to a potentially important shortcoming of the radiation-hydrodynamics simulation.

In the radiation-hydrodynamics calculation it was assumed that X-ray radiative transfer in the wind was a purely absorptive processes. This leads to the presence of an extended wedge around the base of the wind which is only weakly ionized since it is shielded from direct irradiation by a centrally located source. It is in this low ionization material that the radiative line force due to the uv disk photons is most effective in accelerating the flow. However, we have explicitly shown that scattered/reprocessed radiation has a

pivotal role in determining not only the emergent X-ray spectra but also the ionization/thermal conditions in a disk wind. In particular, with our multi-dimensional simulations we find that much of the low density region behind the shielding gas is still rather significantly ionized thanks to scattered light (see Figure 1).

Additional ionization can reduce the line driving, potentially leading to a weaker wind (or even quenching the wind; see Proga 2005). We speculate that the likely consequence of accounting for ionization by scattered X-rays would be that a larger fraction of the material would be in the "failed wind" component whilst less material will be successfully accelerated to escape velocity. To investigate this quantitatively will require further developments of our radiation-hydrodynamics code and additional simulations. We note, however, that for sources accreting close to $\dot{M}_{\rm Edd}$, the formation of the "failed wind" component seems unavoidable and our results suggest that even this alone is an important structure for the formation of the X-ray spectrum. Thus it seems unlikely that structures formed due to the pressure exerted by the uv radiation field of the disk do not play any part in formation of the X-ray spectrum of AGN accreting close to the Eddington limit.

### 4.4 Further work

Important future improvements to the modelling should include investigating how the outflowing gas might continue to affect the spectrum at larger radii and lifting the assumption of axi-symmetry. A fully three-dimensional flow could be more complex and would likely include more density inhomogeneities (see e.g. right panels of fig. 2 in Kurosawa & Proga 2009). This may influence the observables. In particular, optically thick clumps might have a role in explaining hard-band excesses (see e.g. Reeves et al. 2009; Turner et al. 2009). Since both the wind structure and primary X-ray source luminosity are likely to be time-variable, the radiation transport should ultimately be make time-dependent to allow for the calculation of time-lags between spectral features forming in different regions and departures from thermal/ionization equilibrium.

Here, our study has been limited to line-driven winds (as simulated by PK04) but other processes may also contribute to the launching of AGN outflows: e.g. magnetically driven or thermal winds from either an irradiated disk (e.g. Luketic et al. 2010) or an AGN torus (e.g. Dorodnitsyn et al. 2008a,b; Dorodnitsyn & Kallman 2009). Thus, in the future, we will extend our studies to consider alternative wind scenarios and investigate whether there are prospects to discriminate between possible launching mechanisms based on spectroscopic observations. In particular, it will be important to compute spectra based on a magnetically driven disk wind model. It has been shown that magnetic fields could drive a disk wind over a relatively wide range of radii and could explain some of the properties of AGN outflows (Blandford & Payne 1982; Emmering et al. 1992; Contopoulos & Lovelace 1994; Königl & Kartje 1994; de Kool & Begelman 1995; Bottorff et al. 1997, 2000; Everett et al. 2002; Proga 2003; Everett 2005; Fukumura et al. 2010).

## ACKNOWLEDGMENTS

S.A.S acknowledges the University of Nevada, Las Vegas and the Space Telescope Science Institute for hosting visits during which part of this work was carried out. D.P. acknowledges support provided by the *Chandra* award TM0-11010X issued by the *Chandra X-ray Observatory Center*, which is operated by the Smithsonian Astrophysical Observatory for and on behalf of NASA under contract NAS 8-39073. S.A.S. thanks Caroline D'Angelo for several useful discussions.

## REFERENCES

Arav N., Li Z., Begelman M. C., 1994, ApJ, 432, 62
Blandford R. D., Payne D. G., 1982, MNRAS, 199, 883
Blondin J. M., 1994, ApJ, 435, 756
Bottorff M., Korista K. T., Shlosman I., Blandford R. D., 1997, ApJ, 479, 200
Bottorff M. C., Korista K. T., Shlosman I., 2000, ApJ, 537, 134
Braito V., Reeves J. N., Dewangan G. C., George I., Griffiths R. E., Markowitz A., Nandra K., Porquet D., Ptak A., Turner T. J., Yaqoob T., Weaver K., 2007, ApJ, 670, 978
Castor J. I., Abbott D. C., Klein R. I., 1975, ApJ, 195, 157
Contopoulos J., Lovelace R. V. E., 1994, ApJ, 429, 139
de Kool M., Begelman M. C., 1995, ApJ, 455, 448
Dorodnitsyn A., Kallman T., 2009, ApJ, 703, 1797
Dorodnitsyn A., Kallman T., Proga D., 2008a, ApJL, 675, L5
Dorodnitsyn A., Kallman T., Proga D., 2008b, ApJ, 687, 97
Emmering R. T., Blandford R. D., Shlosman I., 1992, ApJ, 385, 460
Everett J., Königl A., Arav N., 2002, ApJ, 569, 671
Everett J. E., 2005, ApJ, 631, 689
Friend D. B., Abbott D. C., 1986, ApJ, 311, 701
Fukumura K., Kazanas D., Contopoulos I., Behar E., 2010, ApJ, 715, 636
Königl A., Kartje J. F., 1994, ApJ, 434, 446
Kurosawa R., Proga D., 2009, ApJ, 693, 1929
Laming J. M., Titarchuk L., 2004, ApJL, 615, L121
Laurent P., Titarchuk L., 2007, ApJ, 656, 1056
Luketic S., Proga D., Kallman T. R., Raymond J. C., Miller J. M., 2010, ArXiv e-prints
Miller L., Turner T. J., Reeves J. N., 2008, A&A, 483, 437
Miller L., Turner T. J., Reeves J. N., George I. M., Kraemer S. B., Wingert B., 2007, A&A, 463, 131
Pauldrach A., Puls J., Kudritzki R. P., 1986, A&A, 164, 86
Pounds K. A., Reeves J. N., 2007, MNRAS, 374, 823
Pounds K. A., Reeves J. N., 2009, MNRAS, 397, 249
Pounds K. A., Reeves J. N., King A. R., Page K. L., O'Brien P. T., Turner M. J. L., 2003, MNRAS, 345, 705
Pounds K. A., Reeves J. N., King A. R., Page K. L., O'Brien P. T., Turner M. J. L., 2005, MNRAS, 356, 1599
Proga D., 2003, ApJ, 585, 406
Proga D., 2005, ApJL, 630, L9
Proga D., Kallman T. R., 2004, ApJ, 616, 688
Proga D., Stone J. M., Kallman T. R., 2000, ApJ, 543, 686
Reeves J. N., O'Brien P. T., Braito V., Behar E., Miller L., Turner T. J., Fabian A. C., Kaspi S., Mushotzky R., Ward M., 2009, ApJ, 701, 493
Ross R. R., Fabian A. C., 2005, MNRAS, 358, 211
Schurch N. J., Done C., 2007, MNRAS, 381, 1413
Schurch N. J., Done C., Proga D., 2009, ApJ, 694, 1
Shu X. W., Yaqoob T., Wang J. X., 2010, ApJS, 187, 581
Sim S. A., 2005, MNRAS, 356, 531
Sim S. A., Long K. S., Miller L., Turner T. J., 2008, MNRAS, 388, 611

Sim S. A., Miller L., Long K. S., Turner T. J., Reeves J. N., 2010, MNRAS, 404, 1369
Stevens I. R., Kallman T. R., 1990, ApJ, 365, 321
Terashima Y., Gallo L. C., Inoue H., Markowitz A. G., Reeves J. N., Anabuki N., Fabian A. C., Griffiths R. E., Hayashida K., Itoh T., Kokubun N., Kubota A., Miniutti G., Takahashi T., Yamauchi M., Yonetoku D., 2009, PASJ, 61, 299
Titarchuk L., Laurent P., Shaposhnikov N., 2009, ApJ, 700, 1831
Turner T. J., Miller L., 2009, A&AR, 17, 47
Turner T. J., Miller L., Kraemer S. B., Reeves J. N., Pounds K. A., 2009, ApJ, 698, 99